Research Square

Preprints are preliminary reports that have not undergone peer review.
They should not be considered conclusive, used to inform clinical practice,
or referenced by the media as validated information.

k-ω SST Based Hybrid RANS/LES of a Supersonic Axisymmetric Base Flow: Validation and Modal Analysis of the Wake

Camille Gouin

camille.gouin@cea.fr

CEA CESTA

Laurent Muscat

CEA CESTA

Marina Olazabal Loumé

CEA CESTA

Research Article

Keywords: Supersonic base flow, Hybrid RANS/LES, Spectral proper orthogonal decomposition, Azimuthal decomposition, Wake dynamics, Helical modes

Posted Date: November 16th, 2026

DOI: https://doi.org/10.21203/rs.3.rs-11561579/v1

License: This work is licensed under a Creative Commons Attribution 4.0 International License.
Read Full License

Additional Declarations: No competing interests reported.

k-ω SST Based Hybrid RANS/LES of a Supersonic Axisymmetric Base Flow: Validation and Modal Analysis of the Wake

Camille Gouin[1*], Laurent Muscat[1] and Marina Olazabal-Loumé[1]

[1]CEA CESTA, 33114 Le Barp, France.

*Corresponding author(s). E-mail(s): camille.gouin@cea.fr;

Abstract

The unsteady near wake of the Mach 2.46 cylindrical afterbody of Herrin and Dutton is simulated at a base-diameter Reynolds number of 2.9 million with a zonal hybrid Reynolds-averaged Navier–Stokes/large-eddy simulation (RANS/LES) approach built on the k-omega shear-stress transport model. An inhibition function based on an expansion-fan sensor releases the boundary-layer shielding at the separation corner, so that the separated shear layer is resolved in LES from its inception. The simulation recovers the measured base pressure and the main features of the mean-velocity and Reynolds-stress distributions, although the recirculation region is about 13 percent too long. The three-dimensional snapshots are analysed with spectral proper orthogonal decomposition of the complex azimuthal Fourier coefficients, which separates the two senses of rotation of each helical wavenumber. An axisymmetric breathing of the recirculation bubble, at Strouhal numbers below 0.05, dominates the fluctuating energy. The antisymmetric shedding, at Strouhal numbers of 0.25 to 0.4, carries equal energy in both senses of rotation and alternates between flapping and helical episodes, consistent with two counter-rotating helical components without a fixed phase relation. Helical structures with azimuthal wavenumbers one to four develop in the recompression region at Strouhal numbers of 0.75 to 1.5, convected at about three quarters of the freestream velocity. Unlike low-Reynolds-number simulations, no preferred four-lobed organisation is found.

Keywords: Supersonic base flow, Hybrid RANS/LES, Spectral proper orthogonal decomposition, Azimuthal decomposition, Wake dynamics, Helical modes

1 Introduction

The flow behind the blunt base of a body in supersonic flight is a canonical, yet still incompletely understood, configuration of compressible turbulence. The low pressure acting on the base can represent a large fraction of the total drag of projectiles, launchers and re-entry vehicles, and the unsteady loads generated in the near wake are a concern for the design of afterbodies and nozzles. The flow topology is well established: the incoming boundary layer separates at the base corner through an expansion fan, a compressible free shear layer develops between the outer supersonic stream and a low-speed recirculation region, and the shear layer is turned back towards the axis through a recompression shock system, where the flow reattaches and the wake develops (Herrin and Dutton 1994). Each of these elements is a source of unsteadiness, and the way they interact governs the base pressure and its fluctuations.

The cylindrical afterbody experiment of Herrin and Dutton (1994) at $M_\infty = 2.46$ has become the reference test case for this flow. It provides mean-velocity and turbulence measurements in the near wake, as well as base-pressure distributions. Planar visualisations by Bourdon and Dutton (1999) later revealed large-scale structures in the shear layer and in the recompression region. In end views, the number of structures around the wake decreases from 10–14 in the recompression region to 4–5 in the developing wake, as the structures amalgamate while the shear layer converges towards the axis; these single-plane, non-time-resolved data, however, could not characterise their dynamics. The case has since been used extensively to assess turbulence-resolving strategies, from detached-eddy simulation (DES) (Forsythe et al. 2002) and hybrid Reynolds-averaged Navier–Stokes/large-eddy simulation (RANS/LES) (Kawai and Fujii 2005) to zonal detached-eddy simulation (ZDES) (Simon et al. 2007). The latter study also identified the main spectral signatures of the wake from point spectra: a low-frequency growing and contracting motion of the recirculation region at $St_D \approx 0.05$, a flapping of the shear layer and an oscillation of the reverse flow at $St_D \approx 0.1$–0.14, and, from the azimuthal decomposition of a ring of sensors in the wake, a helical ($m = 1$) mode at $St_D \approx 0.26$, where $St_D = fD/U_\infty$ is based on the base diameter. More recently, Tian et al. (2024) combined a k-ω shear-stress transport (SST) delayed detached-eddy simulation with dynamic mode decomposition (DMD) to study a Mach 1.96 afterbody with and without an exhaust jet. Without jet, the dominant mode is a low-frequency antisymmetric oscillation of the wake ($St_D \approx 0.1$–0.2). Like earlier studies, however, their modes were extracted in a single meridional plane, which cannot tell a helical motion from a planar one, nor isolate the contribution of higher azimuthal wavenumbers.

In parallel, the three-dimensional organisation of the wake has been studied at lower Reynolds numbers. Sandberg and Fasel (2006) showed, through direct numerical simulation (DNS) of transitional supersonic axisymmetric wakes, that modes with azimuthal wavenumbers $m = 2$ and $m = 4$ play a dominant role in the recompression region, producing four-lobed structures consistent with the visualisations of Bourdon and Dutton (1999). Sandberg (2012) extended this work to turbulent approach flows at $M_\infty = 2.46$ and $Re_D = 10^5$. In these DNS, $m = 1$ dominates the recirculation region and $m = 2$ the developing wake, the four-lobed pattern resulting from $m = 2$ and from its time-steady harmonic $m = 4$. Linear stability analyses of the mean flow

found the axisymmetric mode absolutely unstable and the helical modes $m = 4$–6 the most amplified, shifting to $m = 2$–3 when a turbulent eddy viscosity was included. The near-wake structures were attributed to global instabilities of the wake rather than to upstream conditions. Whether this picture holds at a Reynolds number close to the experimental one, some thirty times higher and with a fully developed turbulent boundary layer at separation, has not been established.

The dynamics of axisymmetric wakes has received more attention in the subsonic and transonic regimes. There, the dominant mechanisms are now well identified: an antisymmetric ($m = 1$) vortex shedding at $St_D \approx 0.2$, a low-frequency pumping or breathing of the recirculation bubble, and very-low-frequency $m = 1$ reorientations associated with the breaking of reflectional symmetry (Deck and Thorigny 2007; Weiss et al. 2009; Rigas et al. 2014; Gentile et al. 2016). Modal decompositions have been instrumental in these findings, from spatio-temporal and modal analyses of high-subsonic base flows (Schrijer et al. 2014) and dynamic mode decomposition of launcher wakes (Statnikov et al. 2017) to spectral proper orthogonal decomposition (SPOD) of the turbulent wake of a disk (Nidhan et al. 2020). In particular, SPOD (Towne et al. 2018; Schmidt and Colonius 2020) combined with an azimuthal Fourier decomposition has become a standard tool for round jets (Schmidt et al. 2018), since it separates mechanisms that share the same frequency but differ in azimuthal organisation. For the present supersonic base flow, the azimuthal content has so far only been examined from point spectra at a single location (Simon et al. 2007); to the authors' knowledge, a field-resolved modal analysis of each azimuthal wavenumber has not yet been carried out at the Reynolds number of the experiments.

Obtaining such data requires resolving the separated shear layer from its inception at a Reynolds number where wall-resolved LES of the approaching boundary layer is prohibitive. Hybrid RANS/LES (HRL) approaches are designed for this situation, as they combine the RANS treatment of attached boundary layers with LES in separated regions (Spalart et al. 1997; Deck and Renard 2020). Their outcome, however, depends critically on where the switch between RANS and LES occurs: a delayed switch leaves the shear layer in a modelled state and alters its instability, which in turn contaminates the whole wake dynamics. Recent developments of ZDES based on the k-ω SST model (Renard et al. 2024) provide a robust shielding of attached boundary layers, together with an inhibition function, built on vorticity gradients, that releases this shielding at separation. In the multi-block structured framework used in the present work, evaluating these higher-order derivatives raised practical difficulties at block interfaces. For supersonic and hypersonic separations, the expansion fan that forms at the separation corner offers an alternative, physically based marker of this location, which only requires first-order velocity derivatives. More generally, the predictive limitations of RANS in high-speed flows (Raje et al. 2025) motivate the use of such approaches in the hypersonic regime, where the present work is a first step.

The objectives of the present paper are therefore twofold. First, an alternative inhibition function based on an expansion-fan sensor is introduced in the k-ω SST ZDES to ensure the switch to LES at the separation corner, and assessed on the Herrin and Dutton configuration. Second, and mainly, the resulting three-dimensional

database is used to characterise the azimuthal organisation of the unsteady near wake at a Reynolds number close to the experimental one. The main contributions are:

- an azimuthal-wavenumber-resolved SPOD of the near wake, performed on the complex azimuthal coefficients so that both senses of rotation are retained, which attributes the breathing, shedding and shear-layer dynamics to distinct wavenumbers and shows that no wavenumber beyond $m = 1$ is energetically preferred;
- a polarisation analysis of the antisymmetric shedding mode, which shows that both senses of rotation carry the same energy and that the motion alternates between flapping and helical episodes, consistent with two counter-rotating helical components without a fixed phase relation rather than with a rotating helix or a flapping motion locked in a fixed plane;
- the identification of a band of helical structures with $|m| = 1$ to 4 in the recompression region and the near wake, whose frequency increases with $|m|$, convected at nearly the same velocity;
- a comparison of the azimuthal content of the near wake with the low-Reynolds-number DNS of Sandberg (2012), which shows that the $m = 2/m = 4$ organisation of the developing wake found at $Re_D = 10^5$ is not retained at a Reynolds number close to the experimental one.

The paper is organised as follows. The HRL method and the proposed inhibition function are described in Sect. 2. The configuration, the numerical set-up and the validation against the experiments are presented in Sect. 3. The spectral analysis and the physical interpretation of the wake dynamics are given in Sect. 4, and conclusions are drawn in Sect. 5.

2 Hybrid RANS/LES methods for supersonic and hypersonic flows

Numerous HRL approaches have been studied for aerodynamic flow cases, from the DES introduced by Spalart et al. (1997) to the more recent continuous eddy simulation (CES) developed by Heinz and Fagbade (2024). For the current study, the ZDES approach of Deck and Renard (2020) has been selected due to its flexibility of use, the handling of the grey area (switch zone between RANS and LES) and its accuracy in separated flow simulation. The recent extension for k-ω SST by Renard et al. (2024) for the type II ZDES seems to be a suitable candidate to simulate a cylinder afterbody flow.

2.1 Use of k-ω SST ZDES II

Contrary to Spalart–Allmaras based HRL methods which use the wall distance, the RANS turbulent characteristic length does not directly appear in the equations. It is defined as

$$L_{\mathrm{RANS}} = \frac{\sqrt{k}}{\beta^* \omega}. \tag{1}$$

In the case of a LES area, this turbulent length is switched to the LES one

$$L_{\mathrm{LES}} = C_{\mathrm{DES}} \Delta_{\mathrm{II}}, \tag{2}$$

where C_{DES} is a model constant, set here to 0.61, and Δ_{II} the cell size computed as a combination of $\Delta_{\max}$ and the vorticity length scale Δ_ω. The dissipation term of the k equation is then replaced by $\rho k^{3/2}/L_t$ where L_t is either L_{RANS} or L_{LES}. When the switch to LES is made, the subgrid scale model corresponds to a transport equation of k.

Considering the case of a separated flow, Renard et al. (2024) introduced new shield functions to protect the boundary layer completely in RANS upstream of the separation point and in LES downstream. Nonetheless, they noticed that an inhibition function is required to annihilate the boundary layer protection at the separation point to ensure the LES use in this area. The latter, denoted $f_R(G_\omega)$ in the following, is computed using a vorticity gradient to identify the shear layer. In the present work, the authors have chosen to ignore the reconstruction of the turbulent viscosity ν_t^R and the vorticity magnitude Ω_{bis}, introduced by Renard et al. (2024), since the irregularity effects of mesh refinement on the SST turbulent profile are not observed in the studied configuration.

2.2 Shielding function for supersonics/hypersonics

The purpose of this section is not to replace $f_R(G_\omega)$, which has been validated on a range of configurations (Renard et al. 2024), but to provide an alternative suited to the present framework. In the multi-block structured solver used here, the vorticity-gradient function requires derivatives of the vorticity, i.e. second derivatives of the velocity, whose evaluation across block interfaces raised practical difficulties and could affect the switch to LES at the separation corner of the afterbody. Another inhibition function is therefore introduced, dedicated to supersonic and hypersonic separated flows. In such cases, near the separation point, an expansion fan is involved and can be used to trigger the inhibition function. Thus, an expansion fan sensor is proposed, inspired by the work of Sciacovelli et al. (2021) on a shock sensor. It combines a Ducros sensor:

$$D = \frac{(\nabla \cdot \mathbf{U})^2}{(\nabla \cdot \mathbf{U})^2 + |\boldsymbol{\omega}|^2}, \tag{3}$$

and the Bhagatwala and Lele (2009) one, modified to detect an expansion fan instead of shock:

$$S_f = \frac{1}{2}\left[1 - \tanh\left(2.5 - \left(10\frac{\delta_x}{c}\right)\nabla \cdot \mathbf{U}\right)\right], \tag{4}$$

with $\boldsymbol{\omega}$ the vorticity, c the speed of sound and δ_x a characteristic length which is set to δ, the boundary layer thickness at the separation point. Then, both sensors are combined, $\phi_f = D \times S_f$, and the new inhibition function is built:

$$f_R(\phi_f) = 1 - \tanh(C_1 \phi_f), \tag{5}$$

with C_1 a constant to determine. This function relies only on the velocity divergence and the vorticity, i.e. on first-order derivatives that are already available in the

solver, so that it does not require the computation of the vorticity gradient and is straightforward to evaluate in a multi-block framework.

3 Cylinder afterbody configuration

This section aims to investigate supersonic separated flow in RANS/LES and validate the use of the inhibition function based on an expansion fan sensor. To that end, the test case of the cylinder afterbody carried out by Herrin and Dutton (1994) is selected. The experiment was run at $M_\infty = 2.46$ (approach velocity 567 m/s, stagnation pressure and temperature 515 kPa and 294 K) and a unit Reynolds number of 52×10^6 m^{-1}, i.e. $Re_D \approx 3.3 \times 10^6$ based on the base diameter $D = 63.5$ mm; it has been used in several studies and offers time-averaged and unsteady data for comparison. The present simulation uses the freestream conditions of Simon et al. (2007): $M_\infty = 2.46$, $U_\infty = 593.8$ m/s, $p_\infty = 31\,415$ Pa and $T_\infty = 145$ K, which give $Re_D \approx 2.9 \times 10^6$.

For the computation, only the rear part of the cylinder is selected, and an inflow boundary condition is set to match the boundary layer thickness of the experiment at the end edge of the cylinder. Particular attention is paid to the structured mesh generation near the shear layer area and then in all the LES zones. To that end, a 164 million-cell grid is generated to carry out the computation. Second-order Heun scheme is selected for time discretization, with a time step of 5×10^{-9} s; the three-dimensional snapshots used in Sect. 4 are extracted every 1000 time steps. Besides, the Koren (1993) slope limiter is used combined with the simple low-dissipation advection upstream splitting method (SLAU) to reach third-order in spatial discretization. No forcing method is used since the sharp corner of the geometry is sufficient to trigger turbulence. The first cell adjacent to the wall lies at $y^+ \lesssim 1$ along the cylinder, where the boundary layer is treated in RANS mode. In the separated shear layer, the vorticity thickness δ_ω of the mean flow is resolved by 80 grid points in the radial direction at $x/R = 0.03$, about 30 around $x/R = 1$ and 45 at $x/R = 2$. The axial and azimuthal spacings are coarser close to separation, $\Delta x/\delta_\omega \approx 0.4$ and $r\Delta\theta/\delta_\omega \approx 0.7$ at $x/R = 0.03$, and fall below $0.2\,\delta_\omega$ for $x/R \gtrsim 1$ as the shear layer thickens. The time step corresponds to a maximum CFL number of 0.5. The mean statistics are averaged over 6 ms, i.e. about 37 convective times L_R/U_∞, the period covered by the three-dimensional snapshots of Sect. 4.

Before computing the whole simulation, the effectiveness of the expansion fan sensor proposed in the present work, is checked. Figure 1 shows the value of the sensor for the current cylindrical afterbody configuration, with the constant C_1 set to 5. The sensor well captures the area corresponding to the expansion fan, immediately after the trailing edge, without any side effects, which validates its definition and implementation.

3.1 Validation against the experiment

Figure 2 underlines the RANS and the LES resolution areas for the current configuration; the switch presented here is time-averaged. The intermediate zones are called grey areas and tend to be minimized. The LES part is pinpointed from the aft region

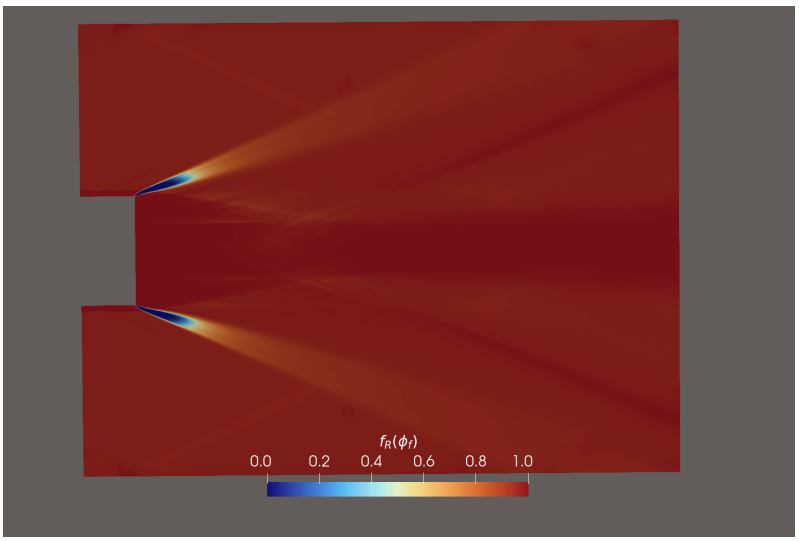


Fig. 1 Expansion fan sensor $f_R(\phi_f)$.

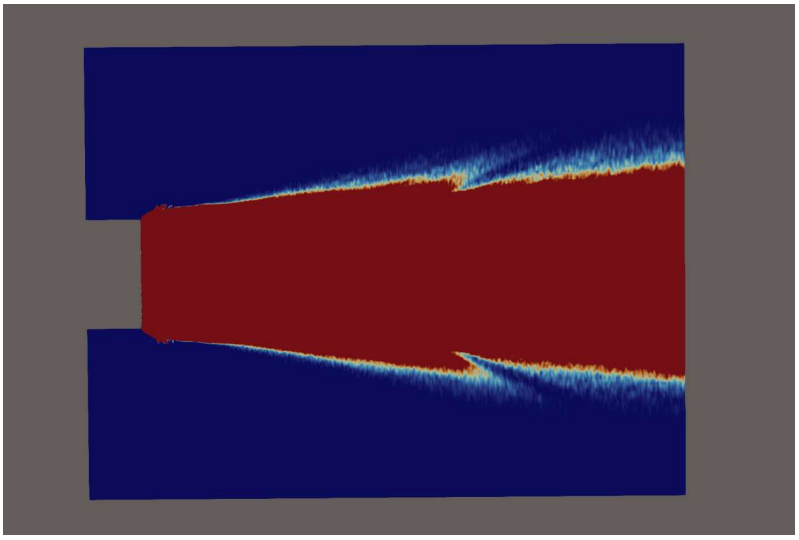


Fig. 2 Time-averaged switch between RANS (blue) and LES (red).

of the cylinder to the output of the wake, which corresponds to the unsteady behavior area of the flow. The upstream part is then, as desired, resolved using the RANS approach.

The length of the recirculating region, defined by the rear stagnation point on the axis of the time- and azimuthally averaged flow, is $L_R \approx 3.0R$ in the HRL computation, against $2.65R$ in the experiment (Herrin and Dutton 1994), i.e. about 13% too long; this point is discussed at the end of this section. The RANS computation,

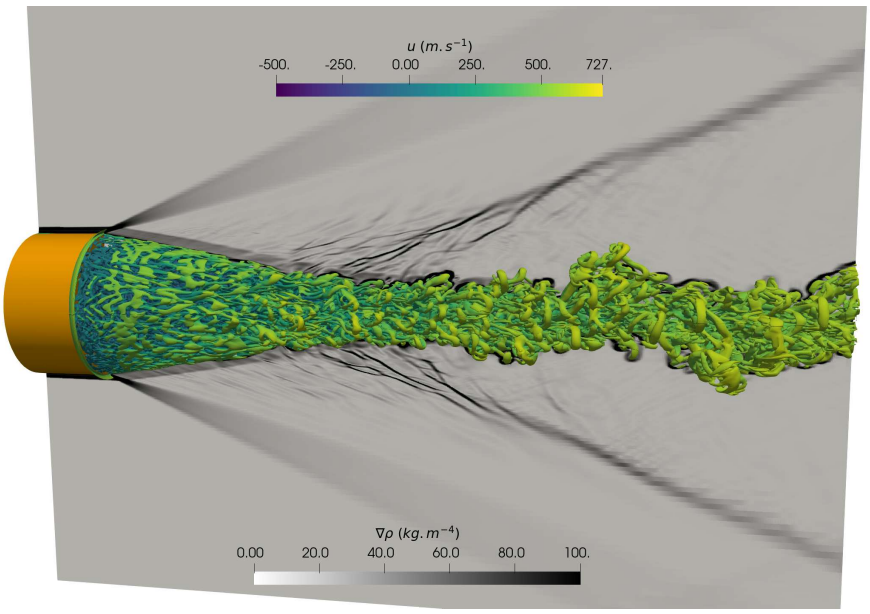


Fig. 3 Instantaneous flow: iso-surface of the Q criterion $Q\,D^2/U_\infty^2 \approx 1.7$ coloured by the streamwise velocity, and magnitude of the density gradient (numerical schlieren) in the meridional plane.

conversely, underestimates the bubble length ($2.18R$), consistently with its too low base pressure. The Q-criterion contour shown in Fig. 3 underlines the abundance of turbulent structures in the flow obtained with the HRL computation, which cannot be captured by RANS method. The unsteadiness is highlighted in the recompression region regarding the density gradient and, on a smaller scale, inside of the shear layer.

The mean base-pressure coefficient, $C_p = (p - p_\infty)/(\frac{1}{2}\rho_\infty U_\infty^2)$ averaged over the base, is -0.105 in the HRL computation, within 3% of the measured value of -0.102 (Herrin and Dutton 1994), whereas the RANS computation with the same k-ω SST model gives -0.143, i.e. a base pressure about 40% too low and a correspondingly overestimated base drag.

Then, the time- and azimuthally averaged streamwise velocity is compared with the measurements of Herrin and Dutton (1994, 1995) at three stations across the separated shear layer, $x/R = 0.03$, 0.095 and 0.158 (i.e. about 1, 3 and 5 mm downstream of the base), in Fig. 4. As expected, the HRL results fit the experimental data better than the RANS ones, which predict a much thicker shear layer. At the first station the HRL profile follows the measurements closely; at the next two, the shear layer is slightly too thin on its low-speed side ($0.93 \lesssim r/R \lesssim 0.97$), where the measured velocity decreases more gradually towards the recirculating flow.

The major improvement of using a HRL method compared to RANS one is, as expected, the capture of unsteadiness. Figure 5 depicts the Reynolds shear stress $\overline{u'u'_r}$ at the same stations. The peak is located at the correct radius at all stations. Its magnitude is underpredicted by about 25% at the first station, recovered at the second,

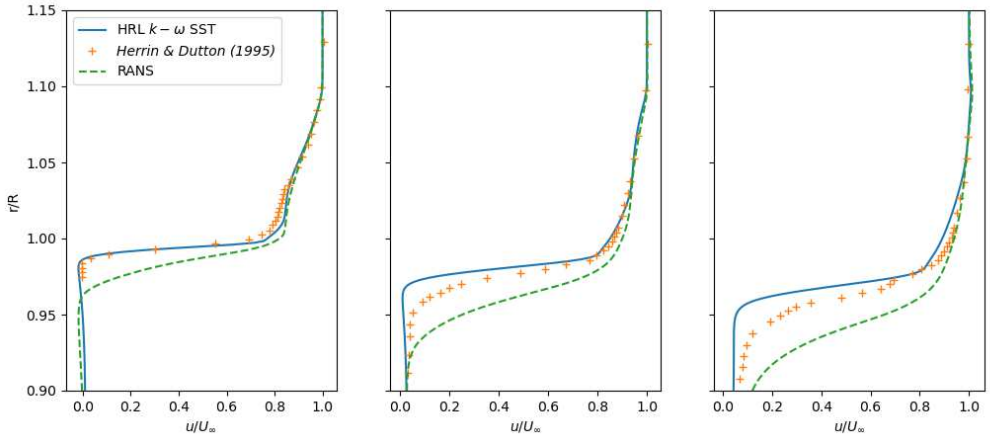


Fig. 4 Time- and azimuthally averaged streamwise velocity u/U_∞ at three stations across the separated shear layer, $x/R = 0.03$, 0.095 and 0.158 (left to right): experimental data of Herrin and Dutton (1995), present HRL and RANS computations.

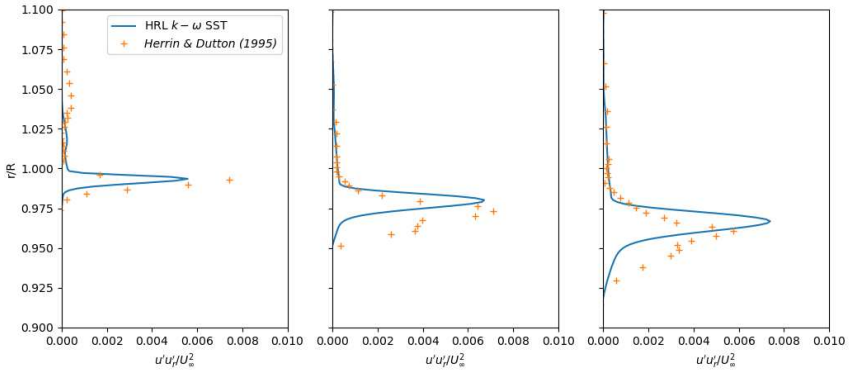


Fig. 5 Time- and azimuthally averaged Reynolds shear stress $\overline{u'u'_r}/U^2_\infty$ at the stations of Fig. 4: experimental data of Herrin and Dutton (1994, 1995) and present HRL computation.

and overpredicted by about 25% at the third, i.e. the HRL shear stress grows faster along the shear layer than in the experiment.

The same trend appears in Fig. 6 for the maximum of the Reynolds shear stress along the shear layer, where both data sets are normalised by the experimental recirculation length, so that the streamwise positions are compared at the same physical location. The streamwise evolution is well reproduced: the shear stress grows along the shear layer, reaches its maximum in the second half of the recirculating bubble, at $x/R \approx 1.9$ against 2.2 in the experiment, and collapses through the recompression region. Close to separation ($x/L_R \leq 0.1$), the experimental values of Fig. 6, taken from Simon et al. (2007), are about twice the peaks of the profiles of Herrin and Dutton (1995) at the same stations (Fig. 5); the two experimental data sets are inconsistent

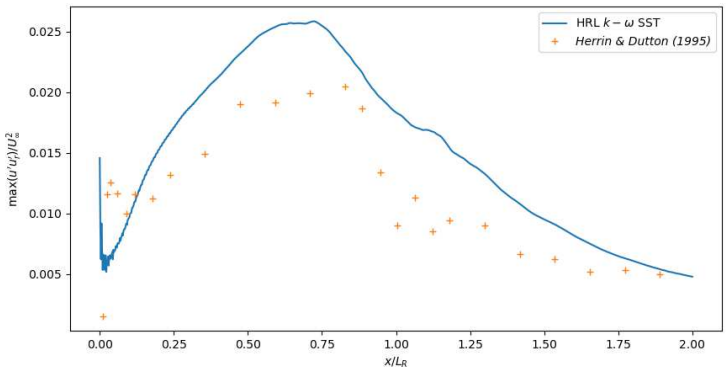


Fig. 6 Maximum over r of the time- and azimuthally averaged Reynolds shear stress as a function of x/L_R, with $L_R = 2.65R$, the experimental recirculation length, for both data sets: experimental data of Herrin and Dutton (1994, 1995), as reported by Simon et al. (2007), and present HRL computation.

there, and the comparison in this region relies on the profiles of Fig. 5. Furthermore, its decay downstream of reattachment is slower than measured. The overprediction could be explained by the subgrid-scale model, the statistical convergence or numerical effects and is discussed in Sect. 5.

The longer recirculating region of the HRL computation, despite an accurate base pressure, is consistent with these observations. The underprediction of the shear stress just downstream of separation points to a slightly delayed development of the resolved turbulence in the first part of the shear layer, a known effect of the transition from modelled to resolved turbulence in hybrid methods. Close to separation, the axial and azimuthal spacings are moreover a significant fraction of the vorticity thickness (Sect. 3), so that the small three-dimensional structures of the initial shear layer are only partly resolved. Both effects delay the entrainment and lengthen the bubble. Accordingly, the maximum reverse velocity on the axis is located further downstream than in the experiment ($x/R \approx 2.1$ against 1.5), with a similar magnitude ($0.32U_\infty$ against $0.27U_1$). Two other factors may contribute. First, the low-frequency breathing of the bubble (Sect. 4.2) is sampled over at most two of its periods, so that the mean position of the rear stagnation point carries a significant statistical uncertainty. Second, the freestream conditions of Simon et al. (2007) differ slightly from those of the experiment ($Re_D \approx 2.9 \times 10^6$ against 3.3×10^6). The HRL computation nevertheless clearly improves on RANS for both quantities, and the base pressure, which governs the base drag, is recovered.

4 Spectral analysis and wake dynamics

4.1 Methodology

The unsteady dynamics of the wake are analysed with SPOD (Towne et al. 2018; Schmidt and Colonius 2020), computed with the Python package PySPOD developed by Mengaldo and Maulik (2021) and Rogowski et al. (2024). SPOD extracts, at each

frequency, the coherent structures that optimally represent the space–time correlation of the flow, and its leading eigenvalue measures the energy of the dominant mechanism at that frequency. A SPOD applied to a meridional plane mixes the contributions of all azimuthal wavenumbers: it cannot tell a helical motion from a planar one, nor whether the structures are axisymmetric. The three-dimensional snapshots are therefore first decomposed into azimuthal Fourier modes, following the approach commonly used for round jets (Schmidt et al. 2018).

Since the configuration is axisymmetric, the flow statistics are homogeneous in the azimuthal direction θ. The fluctuating fields $q' = (u', u'_r, u'_\theta, p')$ are therefore first interpolated onto a cylindrical grid (x, r, θ) with N_θ equally spaced azimuthal stations, and decomposed into azimuthal Fourier modes

$$\hat{q}_m(x, r, t) = \frac{1}{N_\theta} \sum_{k=0}^{N_\theta - 1} q'(x, r, \theta_k, t)\, \mathrm{e}^{-\mathrm{i}m\theta_k}, \tag{6}$$

where m is the azimuthal wavenumber. SPOD can be performed independently for each wavenumber, which yields modes of the form $\boldsymbol{\phi}_m(x, r; St)\, \mathrm{e}^{\mathrm{i}m\theta}$ and energy spectra $\lambda_m^{(j)}(St)$, with j the SPOD mode index. SPOD is performed on the stacked state vector $\hat{\mathbf{q}}_m = (\hat{u}, \hat{u}_r, \hat{u}_\theta, \hat{p})_m$ with the compressible energy norm of Chu (1965), which, for this choice of variables and neglecting entropy fluctuations, reads

$$\langle \mathbf{q}_1, \mathbf{q}_2 \rangle = \int_\Omega \left[\bar{\rho} \left(u_1^* u_2 + u_{r,1}^* u_{r,2} + u_{\theta,1}^* u_{\theta,2} \right) + \frac{p_1^* p_2}{\gamma \bar{p}} \right] r \, \mathrm{d}r \, \mathrm{d}x, \tag{7}$$

where overbars denote mean quantities. A single mode therefore describes all variables consistently, and energies can be compared between wavenumbers.

For $m \neq 0$, the coefficients $\hat{q}_m(t)$ are complex, and the SPOD is performed on the complex signal with a two-sided frequency spectrum, $-f_s/2 < f < f_s/2$. With the conventions of Eq. (6) and a temporal transform in $\mathrm{e}^{-\mathrm{i}2\pi ft}$, a helical structure $\mathrm{e}^{\mathrm{i}(m\theta - 2\pi f_0 t)}$ with $m > 0$, which rotates towards $+\theta$, appears at the negative frequency $f = -f_0$. Positive and negative frequencies of a given $m > 0$ therefore correspond to helical waves of opposite senses of rotation. As the physical fields are real, $\hat{q}_{-m}(t) = \hat{q}_m^*(t)$, so that the spectrum of $(-m, St_D)$ is identical to that of $(m, -St_D)$. Results are therefore presented for positive frequencies and for positive and negative wavenumbers, the sign of m giving the sense of rotation: at $St_D > 0$, $m < 0$ corresponds to a rotation towards $+\theta$ and $m > 0$ to a rotation towards $-\theta$. Comparing m and $-m$ distinguishes a rotating helix from a standing, flapping motion (Sect. 4.3.2). This symmetry was used to validate the processing: the SPOD of $m = -1$, computed independently, reproduces the negative-frequency part of the $m = 1$ spectrum to within 2×10^{-15} (relative), which confirms that the complex coefficients are processed without loss of their imaginary part.

The Strouhal number is based on the base diameter $D = 2R$ and the freestream velocity, $St_D = fD/U_\infty$, so that $St_D = 0.27$ corresponds to $f \approx 2.5$ kHz. Where relevant, a Strouhal number based on the recirculation length, $St_L = fL_R/U_\infty =$

$St_D\,L_R/D$, is also used. The three-dimensional database consists of $N_s = 1200$ snapshots sampled at $\Delta t = 5 \times 10^{-6}$ s, i.e. a total duration of 6 ms, which corresponds to about 37 convective times L_R/U_∞ and 15 periods of the shedding mode. The Welch method is applied with blocks of $N_{\mathrm{fft}} = 600$ snapshots and 50% overlap, i.e. $N_b = 3$ blocks. The frequency resolution is $\Delta f = 1/(N_{\mathrm{fft}}\Delta t) \approx 333$ Hz, i.e. $\Delta St_D \approx 0.036$, and the Nyquist frequency is 100 kHz. All Strouhal numbers given below are those of the discrete frequency bins and are therefore known to within $\pm\Delta St_D/2$. $N_\theta = 64$ azimuthal stations are used, which resolves wavenumbers up to $|m| = 32$; the analysis is carried out for $|m| \leq 16$. Within these wavenumbers, the axisymmetric mode $m = 0$ carries 57% of the fluctuating energy of the azimuthal Fourier coefficients (L^2 norm, $\pm m$ combined), 82% for $|m| \leq 4$ and up to 95% for $|m| \leq 10$, the energy of each wavenumber decreasing steadily to about 0.5% at $|m| = 16$.

With only three blocks, the SPOD eigenvalues are affected by a significant statistical uncertainty: assuming a χ^2 distribution with $2N_b = 6$ degrees of freedom, the 95% confidence interval of a leading eigenvalue spans a factor of about 0.4 to 4.8 around the estimate. Only three SPOD modes exist at each frequency, and only the leading one is expected to be reasonably converged. The analysis below therefore focuses on the location of the spectral peaks, on the spatial structure of the leading modes and on energy differences of one order of magnitude or more, rather than on detailed amplitude ratios. To test the robustness of the results to this choice, the analysis was repeated with blocks of $N_{\mathrm{fft}} = 400$ snapshots ($N_b = 5$, $\Delta f = 500$ Hz, $\Delta St_D \approx 0.053$). With $2N_b = 10$ degrees of freedom, the 95% confidence interval narrows to a factor of about 0.5 to 3.1 around the estimate, and the significance threshold for $\lambda^{(1)}/\lambda^{(2)}$ introduced in Sect. 4.2 drops to about 3.0. The dominant peaks of all wavenumbers are recovered within the frequency resolution; the differences are noted in Sect. 4.2.

4.2 Azimuthal-wavenumber-resolved SPOD

The leading SPOD eigenvalue $\lambda_m^{(1)}$ is mapped in the (St_D, m) plane in Fig. 7(a), the first three eigenvalues of $m = 0, \pm1$ to ±4 are shown in Fig. 7(b)–(d), and the dominant peaks are summarised in Table 1. Each of the first wavenumbers is associated with a distinct frequency range and a distinct region of the flow, which allows each mechanism to be attributed to a wavenumber and a region.

The energy is strongly dominated by the axisymmetric wavenumber: the maximum of $\lambda_0^{(1)}$ over frequency is about twenty times that of $m = 1$, and more than fifty times that of any $m \geq 2$. Beyond $m = 1$, the maximum of $\lambda_m^{(1)}$ decreases smoothly and monotonically with m: relative to $m = 1$, it falls to about 0.34, 0.20 and 0.11 for $|m| = 2$, 3 and 4, 0.07 for $m = 5$, and 0.03 for $m = 8$ (Fig. 7a). No wavenumber beyond $m = 1$ stands out in energy, and in particular no excess is found at $m = 4$ or at its multiples.

Given the small number of blocks, the separation between $\lambda_m^{(1)}$ and $\lambda_m^{(2)}$ is only used qualitatively. A large gap between the first two eigenvalues indicates a low-rank behaviour, i.e. a single coherent mechanism dominating the fluctuations at that frequency (Schmidt et al. 2018). As a rough guide, if the two eigenvalues were independent estimates of the same energy, each following a χ^2 distribution with $2N_b = 6$ degrees of

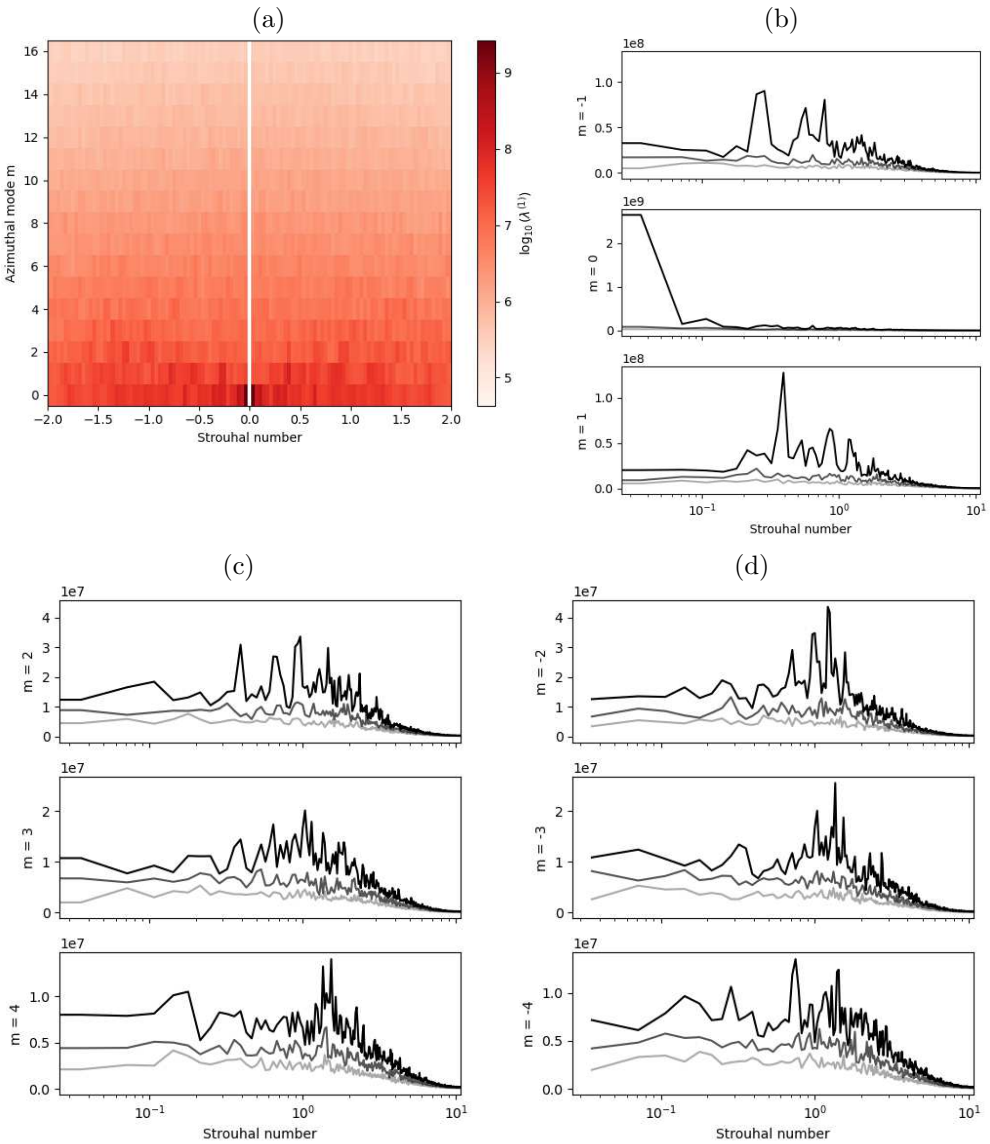


Fig. 7 (a) Leading SPOD eigenvalue $\log_{10}\lambda_m^{(1)}$ as a function of the signed Strouhal number and of the azimuthal wavenumber $m \geq 0$; for $m > 0$, negative Strouhal numbers correspond to $-m$ at positive frequency. (b)–(d) First three SPOD eigenvalues (from dark to light) as a function of St_D for (b) $m = -1$, 0 and 1, (c) $m = 2$ to 4 and (d) $m = -2$ to -4.

Table 1 Dominant SPOD peaks for each azimuthal wavenumber m. The sign of m gives the sense of rotation ($m < 0$: towards $+\theta$). Frequency resolution $\Delta St_D \approx 0.036$; $\lambda^{(1)}/\lambda^{(2)} > 4.3$ is taken as significant.

m	St_D	f (kHz)	$\lambda^{(1)}$ (10^7)	$\lambda^{(1)}/\lambda^{(2)}$	Location of the mode	Proposed mechanism
0	$\lesssim 0.04$	$\lesssim 0.33$	264	31	shear layer, bubble, recompression shocks	bubble breathing (first resolved bin)
0	0.11	1.0	26.5	4.3	bubble (u', u'_r), recompression shocks (p')	low-frequency oscillation of the reverse flow
-1	0.25–0.29	2.3–2.7	8.6–9.1	5.0, 4.8	rear part of bubble and wake ($x/R \gtrsim 2$)	shedding, rotation towards $+\theta$
$+1$	0.36–0.39	3.3–3.7	12.7	9.8	rear part of bubble and wake ($x/R \gtrsim 2$)	shedding, rotation towards $-\theta$
-1, $+1$	0.78, 0.86	7.3, 8.0	8.0, 6.6	8.2, 4.1	recompression region	recompression-region band
$+2$, -2	0.98, 1.21	9.2, 11.3	3.4, 4.4	≤ 5.6	recompression region and near wake	recompression-region band
$+3$, -3	1.04, 1.36	9.7, 12.7	2.0, 2.5	≤ 4.4	recompression region and near wake	recompression-region band
$+4$, -4	1.53; 0.75, 1.36	14.3; 7.0, 12.7	1.4; 1.4, 1.2	4.2; 2.5, 2.5	recompression region	recompression-region band
$\lvert m\rvert \geq 5$	no isolated peak	–	≤ 0.90	≤ 2.8	–	broadband turbulence

freedom, their ratio would remain below about 4.3 with 95% confidence. Only ratios clearly above this value are therefore taken as evidence of such a coherent, low-rank mechanism. This is the case for $m = 0$ at the lowest frequency ($\lambda^{(1)}/\lambda^{(2)} \approx 31$), for $m = 1$ in the shedding band (up to 9.8), and for $|m| = 2$ at high frequency (5.6). For $m = 3$ and 4, the ratio reaches 4.4 and 4.2 in the same band, i.e. at the significance level, and for $m \geq 5$ it never exceeds 2.8. Since about thirty wavenumber–sign combinations and several hundred frequencies are examined, isolated ratios near 4.3 are expected by chance; a peak is therefore retained only when it is also consistent across neighbouring frequencies or wavenumbers.

Axisymmetric mode ($m = 0$).

The $m = 0$ energy (Fig. 7b, Table 1) is concentrated at the lowest resolved frequency, $St_D \approx 0.036$, which coincides with the first frequency bin, with the largest gap between the first two eigenvalues of the whole analysis ($\lambda^{(1)}/\lambda^{(2)} \approx 31$). The actual frequency of this dynamics can therefore only be bounded, $St_D \lesssim 0.04$, and the database covers at most two of its periods. With five blocks, the peak again falls in the first resolved bin, $St_D \approx 0.053$ ($\lambda^{(1)}/\lambda^{(2)} \approx 10$), which coincides with the value found by Simon et al. (2007) near the rear stagnation point; both analyses thus bound the breathing frequency to $St_D \lesssim 0.05$. Being axisymmetric, the corresponding mode describes a pulsation of the recirculation bubble as a whole, i.e. the breathing motion. The mode

(Fig. 8a) involves the whole separated region: u' and u'_r are concentrated along the separated shear layer from the base to reattachment, which moves radially as a whole, u' also has a lobe of opposite sign in the core of the recirculation region ($x/R \approx 1$), and p' is maximum near the rear stagnation point and along the recompression shocks ($2.5 \lesssim x/R \lesssim 5.5$). The breathing therefore couples a radial motion of the shear layer, a change of the reverse flow and a displacement of the recompression shocks. A secondary, marginally significant peak is found at $St_D \approx 0.11$ (1 kHz, ratio 4.3), with an energy ten times lower than that of the breathing but twice that of the shedding peaks. Its velocity components are located inside the recirculation bubble, and its pressure component along the recompression shocks. Its frequency is close to the $St_D \approx 0.1$ activity found by Sandberg (2012) in the separating shear layer. Both $m = 0$ dynamics are discussed in Sect. 4.3.4; their frequencies should be considered with caution until a longer time series is available.

Antisymmetric mode ***($m = 1$).***

For $m = \pm 1$, the energy is concentrated in a band $0.25 \lesssim St_D \lesssim 0.39$: the shedding is carried by the first azimuthal wavenumber. This antisymmetric mode is the dominant large-scale organisation of subsonic, transonic and supersonic axisymmetric wakes (Simon et al. 2007; Weiss et al. 2009; Statnikov et al. 2017; Tian et al. 2024). For the present configuration, Simon et al. (2007) found the $m = 1$ component of the streamwise velocity on a ring of sensors in the wake ($x/R \approx 5.3$) to peak at $St_D \approx 0.26$, within this band and close to the $St_D \approx 0.2$ shedding of low-speed axisymmetric wakes (Canova et al. 2024), whose mode likewise oscillates at the end of the recirculation region (Zhu and Morrison 2021). The corresponding modes (Fig. 8b,c) develop from the rear part of the recirculation region ($x/R \approx 2$, i.e. $x/L_R \approx 0.7$) into the wake, beyond the end of the domain, with u'_r maximum on the axis and p' along the recompression shocks; the $m = +1$ mode, at higher frequency, has a shorter streamwise wavelength. The two senses of rotation therefore occupy the same region, which supports a single shedding mechanism carried by two counter-rotating components. Both senses of rotation carry significant, low-rank energy: the peaks are found at $St_D = 0.25$–0.29 for $m = -1$ ($\lambda^{(1)}/\lambda^{(2)} \approx 5$) and at $St_D = 0.36$–0.39 for $m = +1$ ($\lambda^{(1)}/\lambda^{(2)} \approx 9.8$), and the energy integrated over the band differs by less than 30% between the two senses (ratio 0.72), well within the uncertainty of three-block estimates. Both peaks, and the shift between their frequencies, are recovered with five blocks ($St_D \approx 0.27$ for $m = -1$, $\lambda^{(1)}/\lambda^{(2)} \approx 6.5$; $St_D \approx 0.37$ for $m = +1$, 7.6); this shift is examined in Sect. 4.3.2. Weaker peaks are also visible near $St_D \approx 0.55$ for both senses (Fig. 7b), and two secondary peaks with high ratios are found at $St_D = 0.78$ for $m = -1$ (8.2) and $St_D = 0.86$ for $m = +1$ (4.1), i.e. at roughly twice to three times the shedding frequency. The $m = -1$ peak at $St_D = 0.78$ is nearly as energetic as the shedding peak of the same sense ($\lambda^{(1)} \approx 8.0 \times 10^7$ against 8.6–9.1×10^7). Its mode is not located in the wake but in the recompression region (Fig. 9a), as is the pressure component of the $m = +1$ mode at $St_D = 0.86$, maximum just downstream of the recompression shocks; both belong to the higher-frequency band described below. Their frequencies are close to the difference between those of the $|m| = 2$ band and of the shedding, which suggests a possible nonlinear coupling, but the dominant peaks

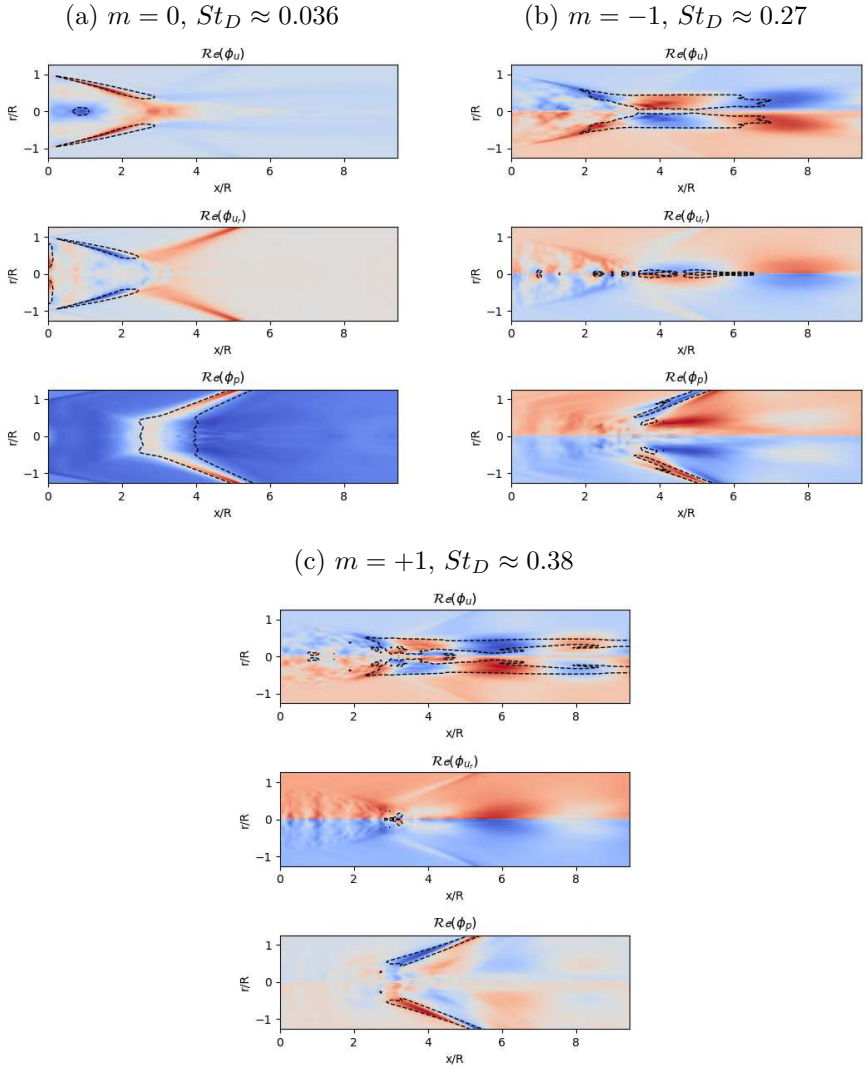


Fig. 8 Streamwise velocity, radial velocity and pressure components (top to bottom) of the leading SPOD modes for (a) $m = 0$ and (b, c) $m = \pm 1$, in the meridional plane $\theta = 0, \pi$. Colours: real part, shown after setting the phase to zero at the maximum of $|u'|$ (each mode is defined up to an arbitrary phase); dashed line: contour of the magnitude at half its maximum. The three components belong to the same mode (Chu norm).

do not satisfy the azimuthal and frequency selection rules of a quadratic interaction, and such couplings could only be established by a bispectral analysis (Schmidt 2020) of a longer time series. Simon et al. (2007) attributed a peak at 8 kHz, found near the location of maximum reverse velocity, to an acoustic resonance of the region enclosed by the sonic line; the present $m = +1$ mode at this frequency lies, however, in the recompression region and not in the reverse flow.

Recompression-region band ($|m| = 1$ to 4).

For $|m| = 2$ to 4, the leading eigenvalue displays a band of low-rank peaks at higher frequency, $St_D \approx 0.75$–1.55,: $St_D = 0.98$ for $m = +2$ and 1.21 for $m = -2$ (best ratio 5.6), 1.04 for $m = +3$ and 1.36 for $m = -3$ (4.4), 1.53 for $m = +4$ (4.2), and, for $m = -4$, two peaks of similar level at $St_D = 0.75$ and 1.36, both below the significance level ($\lambda^{(1)}/\lambda^{(2)} \approx 2.5$) (Fig. 7c,d). Apart from the $m = -4$ peak at 0.75, the frequency of the band increases with $|m|$. All the corresponding modes, as well as the secondary $m = -1$ mode at $St_D = 0.78$, share the same location (Fig. 9; the $m = -4$ modes, not shown, lie in the same region): their amplitude is small along the separated shear layer and reaches its maximum in the recompression region, around and downstream of the rear stagnation point ($2.5 \lesssim x/R \lesssim 5$, $0.2 \lesssim r/R \lesssim 0.5$), where p' is concentrated along and inside the recompression shocks; u' then extends into the developing wake. In three dimensions, these modes are helical waves wrapped around the wake axis (Fig. 10). They are discussed in Sect. 4.3.3.

For $|m| = 2$, the energy is not equally distributed between $m = +2$ and $m = -2$, and the imbalance is of opposite sign to that of $|m| = 1$. With five blocks, the $m = -2$ band is clearly significant ($\lambda^{(1)}/\lambda^{(2)} \approx 5.2$ at $St_D \approx 1.23$ and 4.2 at 0.96) and remains about 1.5 times more energetic than $m = +2$, whose spectrum also shows peaks of comparable level at $St_D \approx 0.38$ and 0.66, the latter significant with five blocks ($\lambda^{(1)}/\lambda^{(2)} \approx 4.5$ at 0.64, with a leading eigenvalue of the same level as that of the 0.98 peak). This mode lies in the same region as the band, u' in the recompression region and u'_r and p' just downstream of the recompression shocks, so that the $m = +2$ contribution to the recompression-region dynamics extends down to $St_D \approx 0.64$. For $m = 3$ and 4, the ratios lie at the significance level in both analyses (4.4 and 4.2 with three blocks; 2.9 and 2.6 with five blocks, against a threshold of 3.0), and the identification of these wavenumbers with the band rests on the location of the modes rather than on the eigenvalue gap alone. In contrast with the low-Reynolds-number DNS (Sect. 4.3.1), $m = 4$ shows no specific dynamics: its energy follows the decay of the neighbouring wavenumbers.

Higher wavenumbers ($m \geq 5$).

Beyond $m = 4$, the spectra no longer display an isolated peak. The frequency at which $\lambda_m^{(1)}$ is maximum varies without trend with m, and the separation between the first two eigenvalues remains small, $\lambda^{(1)}/\lambda^{(2)} \leq 2.8$. With three blocks, such ratios are not significant, and no low-rank mechanism can be identified at these wavenumbers. The streamwise distribution of the energy of each wavenumber (Fig. 11) shows that, for all wavenumbers, the fluctuating energy is maximum in the recompression region and the beginning of the wake ($3 \lesssim x/R \lesssim 5$), $m = 0$ dominating at every station. Along

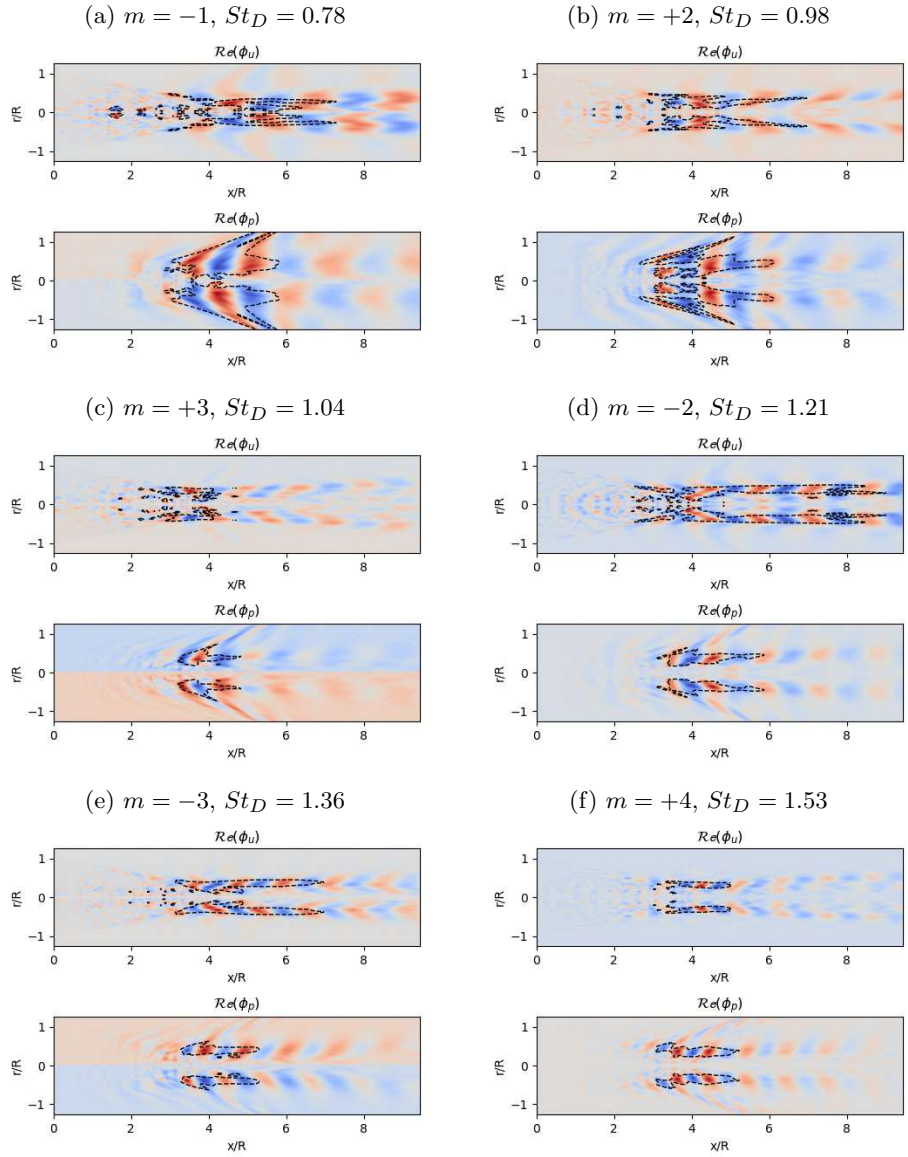


Fig. 9 Streamwise velocity (top) and pressure (bottom) components of the leading SPOD modes of the recompression-region band, ordered by frequency, in the meridional plane $\theta = 0, \pi$. Same representation as in Fig. 8.

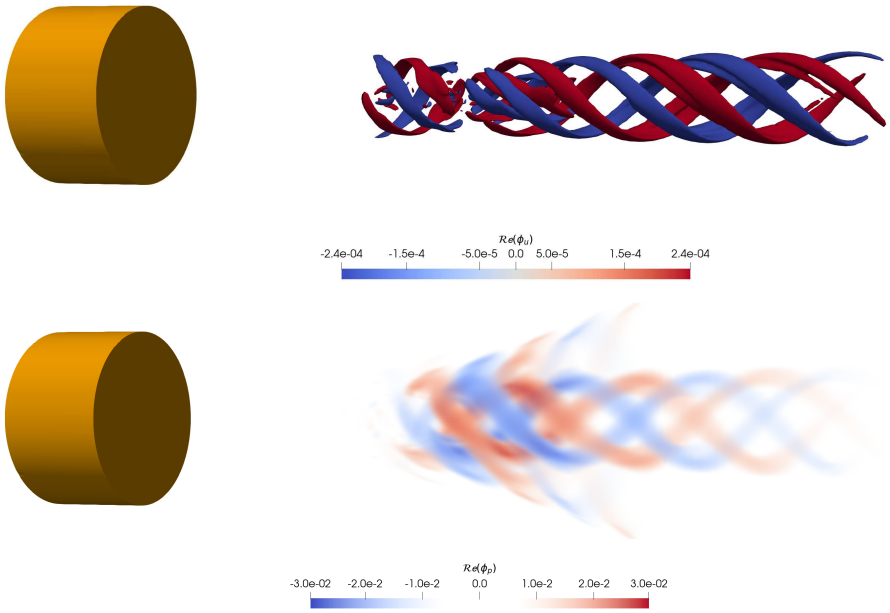


Fig. 10 Three-dimensional view of the leading $m = -2$ SPOD mode at $St_D = 1.21$, $\mathrm{Re}\{\phi\, \mathrm{e}^{-2\mathrm{i}\theta}\}$: iso-surfaces of the streamwise velocity component (top) and pressure component in the meridional and transverse planes (bottom) showing the helical pattern inside the recompression shocks and its imprint along them. The cylinder marks the afterbody.

the first half of the shear layer ($x/R \lesssim 1.5$), the energy of all wavenumbers remains low, and the high wavenumbers only grow from $x/R \approx 2$, i.e. towards reattachment. This absence of coherent structures is not a resolution effect: the computational grid has 360 azimuthal cells, i.e. about 22 cells per wavelength at $m = 16$, and the 64 stations of the interpolation grid resolve wavenumbers up to $m = 32$. Extrapolating the steady decay of the energy per wavenumber beyond $|m| = 16$ (Sect. 4.1), the wavenumbers above 16 carry only a few percent of the fluctuating energy, and the content near $|m| = 32$, which could alias into lower wavenumbers, is negligible. The high-wavenumber content is therefore interpreted as broadband small-scale turbulence rather than as distinct coherent mechanisms, and is not discussed further.

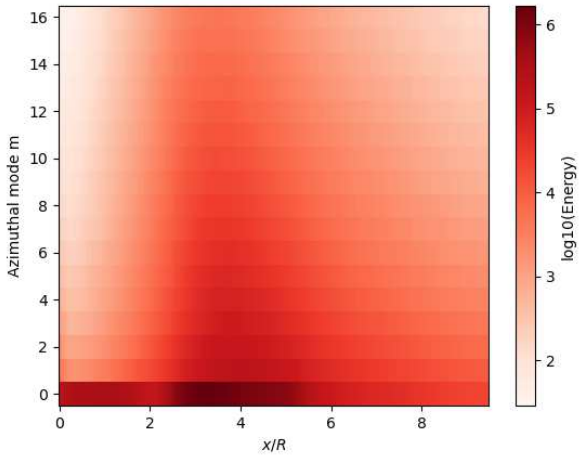


Fig. 11 Streamwise distribution of the time-averaged energy of each azimuthal Fourier mode, integrated over the radial direction ($\log_{10}$ scale), $m = 0$ to 16 computed with the L^2 norm of the state vector. The rear stagnation point is at $x/R \approx 3.0$ in the present computation and 2.65 in the experiment.

4.3 Physical interpretation

4.3.1 Azimuthal content of the near wake and comparison with low-Reynolds-number simulations

The DNS of Sandberg and Fasel (2006) suggested a four-lobed organisation of the recompression region, in which $m = 2$ and $m = 4$ dominate (a preference for even wavenumbers later partly attributed to the symmetry plane imposed by their azimuthal discretisation (Sandberg 2012)), consistent with the 4–5 structures seen in instantaneous end views of the developing wake in the experiment (Bourdon and Dutton 1999); the preferred orientation of these structures, at about $\pm 45°$ from the cardinal axes, was attributed by the authors to a possible slight misalignment of the model, and no mean four-lobed pattern has been reported at the experimental Reynolds number. For turbulent approach flows at $Re_D = 10^5$, Sandberg (2012) found $m = 1$ dominant in the recirculation region and $m = 2$ in the developing wake, the four-lobed pattern being formed by $m = 2$ and its time-steady harmonic $m = 4$; his linear stability analyses give $m = 4$ to 6 as the most amplified modes, or $m = 2$ and 3 when an eddy viscosity is included, and he attributed the wake structure to a global instability of the near wake, largely insensitive to upstream conditions. The present simulation, at a Reynolds number about thirty times higher and with a fully turbulent boundary layer at separation, provides a test of this interpretation.

The unsteady part of the present wake shows no preferred wavenumber beyond $m = 1$: the SPOD energy decays monotonically with m, and $m = 4$ carries no specific dynamics. The possible contamination of the azimuthal content by the four-fold symmetry of the structured grid around the axis was also checked: a grid imprint would be

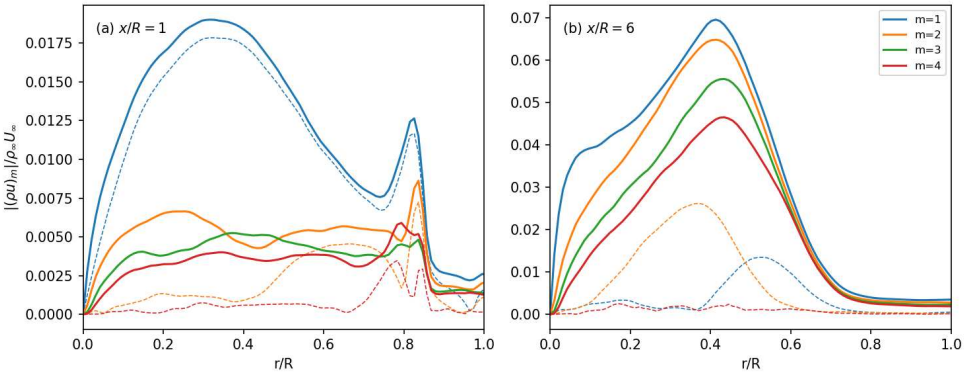


Fig. 12 Time-averaged radial amplitude of the azimuthal Fourier modes of ρu, normalised by $\rho_\infty U_\infty$, at $x/R = 1$ (left) and $x/R = 6$ (right), to be compared with figure 12 of Sandberg (2012). Solid: $\langle|\hat{c}_m|\rangle$, $m = 1$ to 4; dashed: steady part $|\langle\hat{c}_m\rangle|$. Over the present record, a purely fluctuating component leaves a steady part of about 0.2 times its rms in the wake (Sect. 4.3.1).

pinned to the grid, concentrated near the axis and along block interfaces, and would excite all multiples of four, producing excess energy at $m = 4$, 8, 12 and 16. None of these signatures is found, and the smooth decay of $\lambda_m^{(1)}$ with m confirms the absence of such an imprint.

Since SPOD only describes fluctuations about the mean, it does not capture time-steady azimuthal components such as the $m = 4$ harmonic of Sandberg (2012). The comparison is therefore made with the radial amplitude of the azimuthal Fourier modes of ρu at $x/R = 1$ (recirculation region) and $x/R = 6$ (developing wake), as in his figure 12, which shows time-averaged radial amplitudes without specifying whether the time-steady part is separated. Both the mean amplitude $A_m = \langle|\hat{c}_m|\rangle$ and its steady part $S_m = |\langle\hat{c}_m\rangle|$ are therefore shown (Fig. 12), together with the fluctuating part F_m, the rms of $\hat{c}_m - \langle\hat{c}_m\rangle$. Over a finite record, a purely fluctuating component leaves a residual steady part $S_m/F_m \sim N_{\mathrm{ind}}^{-1/2}$, where N_{ind} is the number of independent samples: about 0.2 to 0.26 in the wake, where $N_{\mathrm{ind}} \approx 15$–40, and up to order one in the recirculation region, whose dynamics is much slower.

In the recirculation region, the agreement with the DNS is good: $m = 1$ dominates at all radii, with the same double-peaked radial distribution and a second maximum near $r/R \approx 0.8$, followed by $m = 2$, $m = 3$ coming second only locally around $r/R \approx 0.4$. In the developing wake, by contrast, the amplitude decreases monotonically from $m = 1$ to $m = 6$ ($m = 1$ to 4 shown in Fig. 12), all wavenumbers peaking near $r/R \approx 0.42$: $m = 1$ dominates, instead of $m = 2$ in the DNS. The steady parts confirm this difference. At $x/R = 6$, $S_4/F_4 \approx 0.05$, i.e. there is no time-steady $m = 4$ component, and the steady parts of $m = 1$ and 3 ($S/F \approx 0.17$ and 0.23) are at the noise level. At a Reynolds number close to the experimental one, neither the selection of $m = 2$ nor the steady four-lobed pattern of the DNS is therefore found, in line with the absence of any preferred wavenumber beyond $m = 1$ in the SPOD. This trend is in the direction of the stability analysis of Sandberg (2012), in which an eddy viscosity shifts the most amplified modes towards lower wavenumbers: the higher turbulence

level of the present shear layer appears to damp the selection of a particular azimuthal organisation. The wavenumbers $m = 4$ to 6, the most amplified in his analysis without eddy viscosity, do not appear as distinct coherent structures either.

At $x/R = 1$, the steady part of $m = 1$ is comparable to its fluctuating part ($S_1/F_1 \approx 1.7$), which is within the uncertainty expected over the present record for the slow dynamics of the recirculation region. A similar time-averaged azimuthal content was reported by Sandberg (2012), who attributed it to recurring structures rather than to an asymmetry of the mean flow. At $x/R = 6$, the steady part of $m = 2$ is marginal ($S_2/F_2 \approx 0.38$). A much longer record would be needed to characterise these steady parts, which do not affect the SPOD, computed on fluctuations about the record mean.

4.3.2 Nature of the antisymmetric shedding mode

In subsonic axisymmetric wakes, the $m = 1$ shedding results from the superposition of two counter-rotating helical waves of comparable amplitude (Monkewitz 1988; Sevilla and Martínez-Bazán 2004), which produces a planar, flapping motion whose orientation changes randomly in time (Rigas et al. 2014; Gentile et al. 2016). With the complex SPOD, the two helical components are directly separated by the sign of the frequency. Three scenarios can be distinguished. A rotating helix would carry most of the energy in one sense of rotation. A flapping motion locked in a fixed plane would require two components of equal energy, at the same frequency and with a constant phase relation. Finally, two components with comparable energy but without a fixed phase relation produce a motion that alternates between flapping and helical episodes, with a changing orientation.

The SPOD spectra exclude the first scenario: both senses carry significant, low-rank energy, and their integrated energies differ by less than 30% (Sect. 4.2). To discriminate between the two others, the $m = 1$ coefficient $\hat{c}(t)$ of the radial velocity is band-pass filtered at three probes, separately at positive and negative frequencies, within $\pm 50\%$ of $f_0 = 3$ kHz, i.e. between 1.5 and 4.5 kHz, a band that contains both shedding peaks ($m = -1$ at 2.5 kHz and $m = +1$ at 3.5 kHz). This gives the components $P(t)$ and $N(t)$ rotating in the two opposite senses. The same decomposition into two counter-rotating waves is used to characterise azimuthal thermoacoustic modes in annular combustors, whose state is described by the balance between the two waves (standing or spinning) and by the orientation of the standing part (Ghirardo et al. 2016; Faure-Beaulieu and Noiray 2020). The instantaneous balance between the two components is measured by the ellipticity

$$\varepsilon(t) = \frac{|N|^2 - |P|^2}{|N|^2 + |P|^2} \in [-1, 1], \tag{8}$$

equal to ± 1 for a pure helix and to 0 for a pure flapping motion; the orientation of the flapping plane is set by the phases of P and N, and remains fixed only if they keep a constant phase relation. The results are given in Table 2. At the three probes, the energy ratio between the two senses lies between 0.87 and 1.19 and the mean ellipticity between -0.03 and $+0.05$: within the statistical uncertainty of a record containing about 15 shedding periods (about ± 0.15 on $\langle\varepsilon\rangle$), the two senses of rotation carry

Table 2 Polarisation of the $m = 1$ shedding mode (radial velocity) at three probes. Band 1.5–4.5 kHz. E_-/E_+: energy ratio between the components rotating towards $+\theta$ ($m = -1$) and $-\theta$ ($m = +1$); $\langle\varepsilon\rangle$: mean ellipticity. The last two rows give the theoretical values of two reference scenarios.

x/R	r/R	E_-/E_+	$\langle\varepsilon\rangle$	time with $\lvert\varepsilon\rvert < 0.5$
2.02	0.90	1.13	-0.02	45%
2.69	0.30	1.19	$+0.05$	64%
3.52	0.30	0.87	-0.03	60%
independent helices, equal energy		1	0	50%
stable flapping, fixed plane		1	0	$\approx 100\%$

the same energy. The motion is, however, not a permanent flapping: the flow is in a predominantly flapping state ($|\varepsilon| < 0.5$) during 45 to 64% of the time. This is close to the proportion expected for two independent helical components of equal mean energy, for which ε is uniformly distributed between -1 and 1 (50%, with an uncertainty of about $\pm 13\%$ for the present record), whereas a flapping motion, even with a slowly wandering plane, would give $|\varepsilon| < 0.5$ nearly all the time. Flapping and helical episodes of either sense therefore alternate and, since P and N have no fixed phase relation, the flapping plane is not fixed either. The slightly lower flapping fraction at the probe located in the shear layer ($x/R = 2.02$) is consistent with a larger contribution of broadband turbulence in the filtered band. Such incoherent fluctuations would also give a flapping fraction close to 50%, so that the ellipticity alone cannot distinguish two independent coherent helices from noise; the SPOD, however, shows that both senses of rotation are low-rank in the shedding band ($\lambda^{(1)}/\lambda^{(2)} \approx 5$ to 10, Sect. 4.2), i.e. carried by coherent structures.

The two senses of rotation also peak at different frequencies in the SPOD spectra, $St_D \approx 0.27$ for $m = -1$ and 0.37 for $m = +1$, a shift recovered with both block sizes and therefore not a statistical artefact of the three-block estimates. It cannot result from a uniform azimuthal rotation of the wake, which would displace the frequencies of all wavenumbers in the same direction and proportionally to m, whereas the $|m| = 2$ peaks are displaced in the opposite direction ($m = +2$ below $m = -2$); the mean azimuthal velocity is indeed negligible in the whole domain, except for small values inside the bubble, close to the base and around the location of the maximum reverse velocity. Two counter-rotating waves of different frequencies would make the flapping plane drift slowly, at half their frequency difference. Locally, however, the spectra of the two components overlap strongly, and such a drift cannot be established from the present record.

The antisymmetric shedding therefore carries equal energy in both senses of rotation and alternates between flapping and helical episodes, without a fixed flapping plane. As in subsonic axisymmetric wakes (Rigas et al. 2014), this is consistent with

two counter-rotating helical components of equal energy without a fixed phase relation; these conclusions, obtained at three probes over about 15 shedding periods, should be confirmed with a longer record. The supersonic outer flow and the recompression shock do not appear to modify the nature of this mechanism.

4.3.3 Recompression-region structures

The dynamics of the separated shear layer of this configuration were analysed in detail by Simon et al. (2007), including its growth, the evolution of the Reynolds stresses, its convective Mach number and convection velocity, its azimuthal organisation, with about thirty structures around the azimuth just downstream of separation, and its spectra, which peak at about 60 kHz ($St_D \approx 6$) just downstream of separation and 25 kHz ($St_D \approx 2.7$) ahead of recompression. These features are not revisited here, and the shear layer is only characterised by its convective Mach number (Papamoschou and Roshko 1988)

$$M_c = \frac{U_1 - U_2}{c_1 + c_2}, \tag{9}$$

where subscripts 1 and 2 refer to the high- and low-speed sides, respectively, and $c = \sqrt{\gamma \bar{p}/\bar{\rho}}$. Evaluated at the outer and inner edges of the shear layer in the time- and azimuthally averaged flow, M_c is about 0.9 in the first part of the shear layer and 1.3 near reattachment, in agreement with Simon et al. (2007), who found $M_c > 1$ up to $x/L_R \approx 0.6$ for both their simulation and the experiment.

In the present analysis, the energy of all wavenumbers $|m| \leq 16$ remains low along the first half of the shear layer (Fig. 11), and the low-$|m|$ SPOD modes have only a weak amplitude there (Figs. 8 and 9). This is consistent with the highly three-dimensional vortices of weak azimuthal coherence observed by Simon et al. (2007), and with the experiment, where the tangential velocity fluctuations in the shear layer are the weakest of the three components (Herrin and Dutton 1994). It should, however, be interpreted with caution: the instability waves of this region lie at wavenumbers and frequencies beyond the range analysed here, and the slightly delayed development of the resolved turbulence just downstream of separation (Sect. 3.1) may also reduce the fluctuation level in this region.

The coherent structures of moderate wavenumber ($|m| = 1$ to 4, $St_D \approx 0.75$–1.5) are found in the recompression region, where the shear layer reattaches on the axis, the flow is turned by the recompression shocks and the wake develops (Figs. 9 and 10). This is also where the fluctuating energy of all wavenumbers is maximum (Fig. 11), and where Sandberg and Fasel (2006) and Sandberg (2012) found the $m = 2$ and $m = 4$ structures of their low-Reynolds-number wakes. The streamwise wavelength λ_x of these modes, measured from the phase of their u' component along $r/R = 0.4$ for $3 \leq x/R \leq 5$, is $\lambda_x/R = 1.24$ and 1.70 for $m = -2$ and $+2$, and 1.07 and 1.40 for $m = -3$ and $+3$. The corresponding convection velocities, $U_c = f\lambda_x$, lie between 0.72 and $0.82\,U_\infty$, consistently with the values of 0.6 to $0.8\,U_\infty$ measured by Simon et al. (2007) in this region. The four modes are therefore convected at nearly the same velocity, about $0.75\,U_\infty$, and their frequency is set by their wavelength, $f = U_c/\lambda_x$, which explains why it increases with $|m|$. Unlike the DNS, however, no

single wavenumber is selected, and these structures carry far less energy than the breathing and shedding modes.

4.3.4 Low-frequency dynamics of the recirculation bubble

Expressed with the recirculation length, the upper bound of the $m = 0$ breathing frequency gives $St_L = St_D\, L_R/D \lesssim 0.06$. Low-frequency dynamics of separated regions at such Strouhal numbers, based on the length of the separation, is widely observed. In shock-induced separations, it has been related to a cycle of entrainment by the shear layer and recharge of the separated region, with $St_L \approx 0.03$ (Piponniau et al. 2009). In subsonic axisymmetric separating/reattaching flows, a low-frequency pumping of the bubble at a comparable scaled frequency has been identified (Deck and Thorigny 2007; Weiss et al. 2009), and for the present configuration, Simon et al. (2007) found a peak at $St_D \approx 0.053$ ($St_L \approx 0.07$) in the velocity spectra near the rear stagnation point, which they attributed to a growing and contracting motion of the whole recirculating flow, also seen in the measured base-pressure spectra. The present upper bound, $St_D \lesssim 0.04$, i.e. within one frequency bin of their value, is consistent with this observation. The present value thus falls in the range of the low-frequency breathing of separated flows, which supports an interpretation of the dominant $m = 0$ mode as a mass-exchange (filling/emptying) cycle of the recirculation region, driven by the entrainment of the shear layer and closed at reattachment. Since the frequency of this mode falls in the first resolved bin and the database covers at most two of its periods, this interpretation should be confirmed with a longer sampling. The secondary $m = 0$ peak at $St_D \approx 0.11$ ($St_L \approx 0.17$) is close to the low-frequency activity found by Sandberg (2012) in the separating shear layer at $St_D \approx 0.1$, and to the frequencies $St_D \approx 0.085$–0.14 at which Simon et al. (2007) observed a flapping of the shear layer and an oscillation of the reverse flow. The present mode, however, is not located in the shear layer but inside the recirculation bubble, where it involves both u' and u'_r, with a pressure signature along the recompression shocks. It is therefore closer to the oscillation of the reverse flow than to a flapping of the shear layer, although the motions reported by Simon et al. (2007) appear in the radial and transverse velocity components and are not necessarily axisymmetric. Its origin remains unclear.

4.4 Synthesis of the wake dynamics

The whole recirculation bubble breathes axisymmetrically at low frequency ($St_D \lesssim 0.04$, $m = 0$), at a scaled frequency typical of the filling/emptying of separated regions; this mechanism dominates the fluctuating energy by more than one order of magnitude. The large-scale organisation of the wake is dominated by the antisymmetric shedding mode ($St_D \approx 0.25$–0.39, $m = \pm 1$), which carries equal energy in both senses of rotation and alternates between flapping and helical episodes, as in subsonic wakes. The recompression region and the near wake carry helical structures with $|m| = 1$ to 4 at $St_D \approx 0.75$–1.5, convected at about $0.75\,U_\infty$, whose frequency increases with $|m|$; no coherent low-wavenumber structure is found in the first part of the highly compressible shear layer ($M_c \approx 0.9$–1.3), whose dynamics lie at higher wavenumbers and frequencies (Simon et al. 2007). Beyond $m = 4$, the fluctuations are broadband, and

the energy decreases monotonically with m: in contrast with low-Reynolds-number DNS, no wavenumber beyond $m = 1$ is selected, neither in the fluctuations nor in the time-averaged field.

5 Discussion and conclusion

The unsteady near wake of the Mach 2.46 cylindrical afterbody of Herrin and Dutton has been simulated at a Reynolds number close to the experimental one with a k-ω SST ZDES, and analysed with an azimuthal-wavenumber-resolved SPOD of the three-dimensional snapshots, performed on the complex azimuthal coefficients so that both senses of rotation are retained.

The azimuthal decomposition makes it possible to attribute each mechanism to a given wavenumber and region of the flow. The low-frequency breathing of the recirculation bubble is axisymmetric ($m = 0$, $St_D \lesssim 0.04$, i.e. $St_L \lesssim 0.06$), in the range of the filling/emptying dynamics of separated flows, and carries most of the fluctuating energy. The shedding is carried by the wavenumber $m = 1$ in a band $0.25 \lesssim St_D \lesssim 0.39$, in agreement with previous studies of axisymmetric wakes. Both senses of rotation carry comparable energy, and a polarisation analysis at three probes shows that the motion alternates between flapping and helical episodes: as in the subsonic regime, this is consistent with two counter-rotating helical components of equal energy without a fixed phase relation. Helical structures with $|m| = 1$ to 4 at $St_D \approx 0.75$–1.5, convected at about $0.75\,U_\infty$, develop in the recompression region and the near wake, where low-Reynolds-number DNS found $m = 2$ and 4 structures; no coherent low-wavenumber structure is found in the first part of the compressible shear layer ($M_c \approx 0.9$–1.3). Beyond $m = 4$, the spectra are broadband, and the energy decreases monotonically with m, without the preferred $m = 2$ organisation and the time-steady $m = 4$ component reported in low-Reynolds-number DNS.

These results are obtained with a hybrid method in which the shear layer is resolved in LES from its inception. The inhibition function based on an expansion-fan sensor, used here as an alternative to the vorticity-gradient formulation of Renard et al. (2024), identifies the separation region and ensures the transition from RANS to LES at the separation corner. It exploits a feature that is naturally present in supersonic and hypersonic separated flows, namely the expansion fan generated at the onset of separation, and relies only on first-order derivatives, which makes it straightforward to evaluate in a multi-block structured framework. The base pressure is recovered ($C_p = -0.105$ against -0.102 measured, and -0.143 with RANS), and the Reynolds-stress distributions are correctly located, which indicates that the switch occurs sufficiently early to capture the development of the dominant instability mechanisms. The recirculation region is, however, about 13% longer than measured, whereas RANS underestimates it by 18%.

Some limitations should nevertheless be kept in mind. First, the recirculation length is overestimated by about 13% and the peak Reynolds shear stress by about 27% in the second half of the bubble, which may be related to the subgrid-scale modelling, numerical dissipation, finite sampling effects, the exact location of the RANS-to-LES transition or the axial and azimuthal resolution close to separation. Second, the

three-dimensional database covers 6 ms, i.e. about 37 convective times and 15 shedding periods: the dominant frequency bands and mode shapes are identified, but the eigenvalue estimates carry a significant statistical uncertainty, the $m = 0$ breathing frequency can only be bounded, and the ratios found for $m = 3$ and 4 lie at the significance level. A longer time series would refine these estimates and allow the nonlinear interactions between the identified mechanisms to be tested with a bispectral analysis.

Future work will address these points and extend the analysis in two directions. From a physical perspective, a linear (resolvent or global stability) analysis around the present mean flow would allow the SPOD modes to be related to the amplification mechanisms of the near wake, and would clarify why no wavenumber beyond $m = 1$ is selected at this Reynolds number. From a methodological perspective, the expansion-fan sensor will be applied at higher Mach numbers and on configurations where the accurate prediction of unsteady separation remains a major challenge for current turbulence models (Raje et al. 2025), together with an assessment of the sensitivity of the switching location to the grid resolution, and where the development of compressibility-aware switching criteria may represent an important avenue for improving hybrid RANS/LES methodologies.

Statements and Declarations

Funding

This work was supported by CEA.

Competing interests

The authors have no competing interests to declare that are relevant to the content of this article.

Data availability

The datasets generated and analysed during the current study are not publicly available due to their size and to institutional restrictions, but are available from the corresponding author on reasonable request, subject to approval by CEA.

Code availability

The simulations were performed with an in-house solver developed at CEA, which is not publicly available.

Author contributions

C. Gouin: Conceptualization, Methodology, Software, Investigation, Formal analysis, Visualization, Writing – original draft. L. Muscat: Supervision, Writing – review and editing. M. Olazabal-Loumé: Supervision, Writing – review and editing. All authors read and approved the final manuscript.

Ethics approval, consent to participate and consent for publication

Not applicable.

References

Bhagatwala A, Lele SK (2009) A modified artificial viscosity approach for compressible turbulence simulations. Journal of Computational Physics 228:4965–4969. https://doi.org/10.1016/j.jcp.2009.04.009

Bourdon CJ, Dutton JC (1999) Planar visualizations of large-scale turbulent structures in axisymmetric supersonic separated flows. Physics of Fluids 11(1):201–213. https://doi.org/10.1063/1.869913

Canova A, Zhu T, Morrison JF (2024) Control of a bluff body wake using travelling jets. International Journal of Heat and Fluid Flow 110:109605. https://doi.org/10.1016/j.ijheatfluidflow.2024.109605

Chu BT (1965) On the energy transfer to small disturbances in fluid flow (Part I). Acta Mechanica 1(3):215–234. https://doi.org/10.1007/BF01387235

Deck S, Renard N (2020) Towards an enhanced protection of attached boundary layers in hybrid RANS/LES methods. Journal of Computational Physics 400:108970. https://doi.org/10.1016/j.jcp.2019.108970

Deck S, Thorigny P (2007) Unsteadiness of an axisymmetric separating-reattaching flow: numerical investigation. Physics of Fluids 19:065103. https://doi.org/10.1063/1.2734996

Faure-Beaulieu A, Noiray N (2020) Symmetry breaking of azimuthal waves: slow-flow dynamics on the Bloch sphere. Physical Review Fluids 5(2):023201. https://doi.org/10.1103/PhysRevFluids.5.023201

Forsythe JR, Hoffmann KA, Cummings RM, et al (2002) Detached-eddy simulation with compressibility corrections applied to a supersonic axisymmetric base flow. Journal of Fluids Engineering 124(4):911–923. https://doi.org/10.1115/1.1517572

Gentile V, Schrijer FFJ, van Oudheusden BW, et al (2016) Low-frequency behavior of the turbulent axisymmetric near-wake. Physics of Fluids 28:065102. https://doi.org/10.1063/1.4953150

Ghirardo G, Juniper MP, Moeck JP (2016) Weakly nonlinear analysis of thermoacoustic instabilities in annular combustors. Journal of Fluid Mechanics 805:52–87. https://doi.org/10.1017/jfm.2016.494

Heinz S, Fagbade A (2024) Continuous eddy simulation (CES): conceptual approach and applications. In: Proceedings of the 13th International Symposium on Turbulence and Shear Flow Phenomena (TSFP13), Montreal, https://doi.org/10.48550/arXiv.2411.19834, arXiv:2411.19834

Herrin JL, Dutton JC (1994) Supersonic base flow experiments in the near wake of a cylindrical afterbody. AIAA Journal 32(1):77–83. https://doi.org/10.2514/3.11953

Herrin JL, Dutton JC (1995) Effect of a rapid expansion on the development of compressible free shear layers. Physics of Fluids 7(1):159–171. https://doi.org/10.1063/1.868737

Kawai S, Fujii K (2005) Computational study of a supersonic base flow using hybrid turbulence methodology. AIAA Journal 43(6):1265–1275. https://doi.org/10.2514/1.13690

Koren B (1993) A robust upwind discretisation method for advection, diffusion and source terms. In: Vreugdenhil CB, Koren B (eds) Numerical Methods for Advection–Diffusion Problems. Vieweg, Braunschweig, p 117–138

Mengaldo G, Maulik R (2021) PySPOD: a Python package for spectral proper orthogonal decomposition (SPOD). Journal of Open Source Software 6(60):2862. https://doi.org/10.21105/joss.02862

Monkewitz PA (1988) A note on vortex shedding from axisymmetric bluff bodies. Journal of Fluid Mechanics 192:561–575. https://doi.org/10.1017/S0022112088001983

Nidhan S, Chongsiripinyo K, Schmidt OT, et al (2020) Spectral proper orthogonal decomposition analysis of the turbulent wake of a disk at $Re = 50\,000$. Physical Review Fluids 5:124606. https://doi.org/10.1103/PhysRevFluids.5.124606

Papamoschou D, Roshko A (1988) The compressible turbulent shear layer: an experimental study. Journal of Fluid Mechanics 197:453–477. https://doi.org/10.1017/S0022112088003325

Piponniau S, Dussauge JP, Debiève JF, et al (2009) A simple model for low-frequency unsteadiness in shock-induced separation. Journal of Fluid Mechanics 629:87–108. https://doi.org/10.1017/S0022112009006417

Raje P, Parish E, Hickey JP, et al (2025) Recent developments and research needs in turbulence modeling of hypersonic flows. Physics of Fluids 37(3):031304. https://doi.org/10.1063/5.0253703

Renard N, Vaquero J, Gand F, et al (2024) A fully automatic and robust hybrid Reynolds-averaged Navier–Stokes/large eddy simulation approach based on the Menter shear stress transport k–ω model. Physics of Fluids 36(11):115160. https://doi.org/10.1063/5.0222762

Rigas G, Oxlade AR, Morgans AS, et al (2014) Low-dimensional dynamics of a turbulent axisymmetric wake. Journal of Fluid Mechanics 755:R5. https://doi.org/10.1017/jfm.2014.449

Rogowski M, Yeung BCY, Schmidt OT, et al (2024) Unlocking massively parallel spectral proper orthogonal decompositions in the PySPOD package. Computer Physics Communications 302:109246. https://doi.org/10.1016/j.cpc.2024.109246

Sandberg RD (2012) Numerical investigation of turbulent supersonic axisymmetric wakes. Journal of Fluid Mechanics 702:488–520. https://doi.org/10.1017/jfm.2012.201

Sandberg RD, Fasel HF (2006) Numerical investigation of transitional supersonic axisymmetric wakes. Journal of Fluid Mechanics 563:1–41. https://doi.org/10.1017/S0022112006000899

Schmidt OT (2020) Bispectral mode decomposition of nonlinear flows. Nonlinear Dynamics 102:2479–2501. https://doi.org/10.1007/s11071-020-06037-z

Schmidt OT, Colonius T (2020) Guide to spectral proper orthogonal decomposition. AIAA Journal 58(3):1023–1033. https://doi.org/10.2514/1.J058809

Schmidt OT, Towne A, Rigas G, et al (2018) Spectral analysis of jet turbulence. Journal of Fluid Mechanics 855:953–982. https://doi.org/10.1017/jfm.2018.675

Schrijer FFJ, Sciacchitano A, Scarano F (2014) Spatio-temporal and modal analysis of unsteady fluctuations in a high-subsonic base flow. Physics of Fluids 26(8):086101. https://doi.org/10.1063/1.4891257

Sciacovelli L, Passiatore D, Cinnella P, et al (2021) Assessment of a high-order shock-capturing central-difference scheme for hypersonic turbulent flow simulations. Computers & Fluids 230:105134. https://doi.org/10.1016/j.compfluid.2021.105134

Sevilla A, Martínez-Bazán C (2004) Vortex shedding in high Reynolds number axisymmetric bluff-body wakes: local linear instability and global bleed control. Physics of Fluids 16(9):3460–3469. https://doi.org/10.1063/1.1773071

Simon F, Deck S, Guillen P, et al (2007) Numerical simulation of the compressible mixing layer past an axisymmetric trailing edge. Journal of Fluid Mechanics 591:215–253. https://doi.org/10.1017/S0022112007008129

Spalart PR, Jou WH, Strelets M, et al (1997) Comments on the feasibility of LES for wings, and on a hybrid RANS/LES approach. In: Advances in DNS/LES, Proceedings of the 1st AFOSR International Conference on DNS/LES. Greyden Press, Columbus, OH, pp 137–147

Statnikov V, Meinke M, Schröder W (2017) Reduced-order analysis of buffet flow of space launchers. Journal of Fluid Mechanics 815:1–25. https://doi.org/10.1017/jfm.2017.46

Tian YY, Shen LH, Gao ZX, et al (2024) Unsteady characteristics of supersonic base flow influenced by the exhaust jet. Physics of Fluids 36(9):095135. https://doi.org/10.1063/5.0221657

Towne A, Schmidt OT, Colonius T (2018) Spectral proper orthogonal decomposition and its relationship to dynamic mode decomposition and resolvent analysis. Journal of Fluid Mechanics 847:821–867. https://doi.org/10.1017/jfm.2018.283

Weiss PE, Deck S, Robinet JC, et al (2009) On the dynamics of axisymmetric turbulent separating/reattaching flows. Physics of Fluids 21:075103. https://doi.org/10.1063/1.3177352

Zhu T, Morrison JF (2021) Simulation of the turbulent axisymmetric bluff body wake with pulsed jet forcing. Physical Review Fluids 6:124604. https://doi.org/10.1103/PhysRevFluids.6.124604